Proceedings of the Eighth Symposium on the Art of Glass Blowing (The American Scientific Glass Blowers Society, Wilmington, Del., 1963), p. 136.
[45]R. D. Hancock and S. Edelman, Rev. Sci. Instrum. **27**, 1082 (1956); see also J. W. Edwards, Semicond. Prod. **6**, 30 (1963); Semicond. Prod. **6**, 34 (1963).
[46]Type *A* Preamplifier and Model HR-8 Lock-in Amplifier, Princeton Applied Research Corp., P. O. Box 565, Princeton, N.J.
[47]A. Onton, Ph.D. thesis (Purdue University, 1967) (unpublished).
[48]A. Savitsky and M. J. E. Golay, Anal. Chem. **36**, 1627 (1964).
[49]W. H. Kleiner, MIT Lincoln Laboratory, Quarterly Report, Solid State Research, November 1958, p. 54 (unpublished).
[50]J. C. Hensel and K. Suzuki, in Ref. 11, p. 541.
[51]J. J. Stickler, H. J. Zeiger, and G. S. Heller, Phys. Rev. **127**, 1077 (1962).
[52]S. Rodriguez, P. Fisher, and F. Barra, Phys. Rev. B **5**, 2219 (1972).
[53]A comparison of LCW's results for the D line and $E_{||}$ (see Fig. 2 of Ref. 32) and those given in Table II shows that the ratio of the intensities of the two pairs of D components for $E_{||}$ is about 6.74, thus giving $v_D \simeq \pm 3/8$. The ambiguity in the sign of v_D is due to the different transitions in Ref. 32 not being identified. A similar comparison for $E_\perp$ of the four D components of equal intensity gives $u_D \simeq 1/6$, a value which is compatible with the intensities of the remaining $E_\perp$ components and the above value of v_D. A comparison, in a like manner, of the G components in Fig. 2 of LCW gives the values for u_G and v_G. It should be noted that if the two weak G components for $E_\perp$ were of zero intensity then u_G and $|v_G|$ would be exactly 8/9 and 1/3, respectively.
[54]In reaching these conclusions, it was assumed that D_8 is of larger energy than D_7 although within the experimental error these appear to have the same linear Zeeman shift.
[55]It might be noted that the errors in these values of g_1^D and g_2^D are substantially smaller than those given in Table VIII. This simply reflects the fact that the most probable errors in this case are smaller than the difference between the average $E_\mu - E_{-\mu}$ and each individual $E_\mu - E_{-\mu}$.
[56]If this is a correct representation of the behavior of D_4, it is difficult to understand in view of the prominence of this component. The accuracy with which the energy of this component can be determined appears to preclude this possibility.
[57]In this calculation the quantities given in Eqs. (9) contain the values of p' and p^D. Since these each lie close to the idealized case it is assumed that the combination of g_2' and g_2^D obtained here and later are relatively independent of the values of p' and p^D.

PHYSICAL REVIEW B VOLUME 8, NUMBER 2 15 JULY 1973

Energy and Temperature Dependence of Low-Energy-Electron Diffraction from Xenon Single Crystals*

A. Ignatiev† and T. N. Rhodin
School of Applied and Engineering Physics, Cornell University, Ithaca, New York 14850
(Received 5 January 1973)

A complete set of intensity-energy spectra as a function of electron energy, crystal temperature, and incidence angle have been measured for the specular and the first-order nonspecular beams for the (111) xenon surface. The xenon single crystals were formed by epitaxial deposition onto a (100) iridium substrate and were of excellent order and purity. The character of the intensity-energy spectra indicated xenon to be a highly kinematic electron scattering material. Hence the formalism for kinematic scattering could be applied with confidence to the analysis of electron scattering in xenon and with specific reference to the surface dependence of the effective Debye temperature and to surface-layer thermal expansion.

I. INTRODUCTION

Since the inception of low-energy-electron diffraction (LEED) by Davisson and Germer in 1927,[1] it has been indicated that LEED would be able in principle to describe the atomic positions, electronic structure, and vibrational properties of surfaces of single crystals similarly to those of x-ray diffraction for the bulk. Complete analysis of a typical LEED spectra, however, has proved to be a formidable problem because of the occurrence of multiple scattering associated with the very strong interaction of the electrons with the atoms. Recently model calculations in which such events are considered in terms of formal scattering theory have shown good agreement with experiment. These computations are involved and time consuming using $\frac{1}{2}$–4 h of computer time on large computers.[2–4] Therefore, the application of such calculations to the solution of the surface structure and surface properties of specific electron scattering systems at the present time does not provide as yet a routine procedure for structure analysis.

One way of simplifying the problems of a complete multiple scattering analysis is to analyze the electron scattering data in the kinematic scattering formalism. This, however, leads to realistic results only for systems that truly exhibit kinematic features. For electron scattering from most crystalline solids such systems are not typical because

of the very strong interaction of electrons with solids as previously indicated. However, if the scattering conditions are such that the elastic electron scattering potential is weak, and inelastic processes are strong, kinematic scattering can be realistically used[6] to define the scattering process.

In the LEED energy range 10–500 eV, inelastic electron scattering is relatively strong and primarily due to plasmon and electron-hole excitations. General considerations indicate that it does not vary by more than a factor of 2 from one material to another.[5] Elastic electron scattering is governed primarily by the ratio of the atomic scattering factor to the size of the unit cell of the target material. Since atomic scattering factors do not vary by more than a factor of 2 for most elements,[6] the strength of the elastic scattering from an elemental solid is primarily dependent on the unit cell size. For this reason an elemental solid with a very large unit-cell size is expected to exhibit relatively weak elastic scattering.

A class of materials conforming to the above considerations, and hence likely to exhibit strong kinematic electron scattering, are the heavier inert-gas solids xenon, krypton, and argon. The inert-gas solids are also of particular interest from the viewpoint of electron scattering because of the possibility of correlating data on thermal scattering with published theoretical calculations of surface-atom mean-square vibration amplitudes obtained by assuming a Lennard–Jones (6–12) interatomic potential.[7-9]

Of the inert-gas solids, xenon, which possesses the largest unit cell size, $a_0 = 6.173$ Å at 55 °K, and hence the smallest elastic scattering, is expected to exhibit the highest degree of kinematic scattering. In addition, its relatively low vapor pressure and high melting point make it most appropriate to study experimentally. However, the xenon melting point of 161 °K is relatively low and presents some difficulties in the preparation of single-crystal samples suitable for experimental study.

The low xenon melting point indicates *in situ* epitaxial growth is a promising approach for the preparation of single-crystal surfaces for LEED investigation. Several authors have reported studies relevant to the growth and structure of inert-gas crystals deposited on substrates.[10–15] Venables and Ball[10,11] have grown xenon crystals on graphite and observed their nucleation, structure, and orientation with electron microscopy. Dickey, Farrell, and Strongin[14] and Farrell, Strongin, and Dickey[15] have grown single-crystalline argon films and xenon and krypton crystals on Nb (100) and have observed the resulting LEED diffraction patterns and inelastic-loss spectra. However, it was not possible for the latter to achieve a complete LEED intensity analysis for these crystals.

In this study, a systematic investigation of the LEED spectra from epitaxially grown crystalline xenon as a function of energy, scattering direction, and temperature was achieved. In Sec. II, the experimental apparatus and experimental procedures are briefly described. The epitaxial growth of xenon on Ir(100), and the crystal thickness, order, and purity are covered in Sec. III. Section IV presents the xenon (111) LEED intensity-energy spectra for the specular and nonspecular beams and describes the kinematic character of the scattering. Contributions from thermal scattering are discussed in Sec. V.

II. EXPERIMENTAL APPARATUS AND PROCEDURE

The growth and the study of the xenon single crystals was performed in an ultra-high-vacuum (UHV) chamber equipped with LEED gun and four-grid optics, a glancing-incidence Auger gun, a mass spectrometer, a low-temperature crystal manipulator, and a spot photometer. A complete description of the system has been presented previously.[16,17]

Routine preparation of high-quality xenon single crystals and measurement of low-energy-electron scattering were performed. The main body of experimental data consisted of plots of the elastically scattered electron intensity over a range of temperature as a function of incident electron energy for many different angles of scattering. The elastically scattered intensity is critically dependent on many factors. Such factors consist of both those inherent in the electron scattering process at the surface of the material (e.g., surface contaminant effects, surface roughness effects, surface order, and thermal effects), as well as those dependent on the instrumental aspects of the measurements, e.g., control of magnetic and electric fields, determination of sample temperature and orientation, and monitoring of the diffracted intensity. The latter procedural factors are those which generally produce possible errors in the experimental determination of LEED intensity-energy spectra. In this study, these factors were very carefully considered[17] and possible experimental errors are described.

Since the intensity-energy spectra were obtained by the spot-photometer fluorescent-screen method and normalized electronically *in situ* to changes in the incident electron current, the total error in the measured intensity was determined to be ± 5% over the sampled 10–500 eV energy range of the measurement. This value is a conservative estimate since for any one xenon crystal, the differences in the reproducibility of the measured intensities for different spectra never exceeded 3–4%. The angle of incidence of the intensity-energy spectra was

reproducible to within ±1°. The absolute temperature of the xenon crystals in the 50–80 °K temperature range used in the study was defined to within ±1 °K, while the relative temperature was defined to within ±0.1 °K.

III. XENON CRYSTAL GROWTH, ORDER, AND COMPOSITION

The xenon single crystals were grown epitaxially on a carefully prepared and characterized iridium (100) surface using research-grade xenon gas. The major contaminant in the xenon gas was krypton at less than 10 ppm. All other contaminants were present at less than 2 ppm. The crystals were grown in a fcc structure with a (111) surface orientation. The growth procedures and observed epitaxy of xenon corresponding to the two allotropic surface structures of the iridium (100) surface (1×1 and 1×5) have been described previously by Ignatiev, Jones, and Rhodin.[16]

A. Xenon Crystal Thickness

The thickness of the xenon crystals was determined both from analysis of adsorption isotherm relationships and by Auger spectroscopy. The xenon crystals were initially grown at 56 °K at a xenon pressure of 1×10^{-7} Torr. Upon increasing the temperature, the xenon background pressure was likewise incrementally increased to a limiting value of 2×10^{-6} Torr at 74 °K. The xenon coverage on the iridium substrate, i.e., the xenon crystal thickness, could therefore be determined from published absorption data for known values of the equilibrium xenon gas pressure and the absorption temperature of the crystal. The published adsorption isotherms are available for xenon absorption on Pyrex, molybdenum, and tungsten at 90.2 and 77.3 °K.[18,19] They are of the Dubin–Radushkevich form, which is somewhat substrate dependent but relatively temperature independent. Extrapolation of the isotherms's data to various adsorption temperatures was therefore readily achieved. The data on xenon coverage or crystal thickness obtained in this manner are shown in Table I. These coverage estimates indicate that, except for temperatures greater than 72 °K, the xenon crystal thickness was greater than about eight monolayers and that over the studied temperature range 50–80 °K, the crystals were relatively thick, with a typical thickness of 20 to 30 layers.

The absorption isotherm determinated xenon coverages were independently checked by monitoring xenon-Auger-peak intensities as a function of xenon exposure and then correlating the exposure with coverage. The behavior of four typical xenon Auger peaks as a function of xenon exposure is shown in Fig. 1. The exposure in Langmuirs was

TABLE I. Xenon crystal thickness in specific temperature and xenon gas background pressure ranges used in the experiment. The thickness was deduced from xenon adsorption isotherms of Refs. 17 and 18.

Temp. range (°K)	Background pressure (Torr)	P/Po	Thickness (monolayers Xe)
55–50	1×10^{-7}	0.3–0.03	50–18
60–64	5×10^{-7}	0.2–0.03	40–18
64–70	1×10^{-6}	0.05–0.005	20–8
70–74	3×10^{-6}	0.02–0.004	15–6

determined from ion gage measurements that were calibrated for the xenon ionization cross section.[20] (One Langmuir corresponds to 1×10^{-6} Torr of gas for 1 sec and the abbreviation is L.) The calibration of exposure to coverage was determined from the observed 3×5 diffraction pattern during the initial stages of xenon crystal growth on the iridium (100) 1×5 surface.[16] Formation of the 3×5 pattern was very sensitive to xenon exposure in that the features of the LEED pattern noticeably altered for an exposure different from the optimum 0.8 L by as little as ≈0.25 L. The proposed interpretation of the 3×5 LEED structure corresponded to a xenon surface coverage of approximately 0.2 monolayers. When correlated with the 0.8-L exposure this yielded the relationship that a xenon monolayer was equivalent to approximately 4 L or 6.9×10^{14} atoms/cm^2.[20] This result compares very well with the (111) xenon monolayer concentration of 6.1×10^{14} atoms/cm^2, and gives support to the exposure-coverage correlation. This calibration based on Auger electron emission, however, is valid only in the linear region of the Auger electron intensity versus exposure curve since it is in this region that the xenon sticking probability is unity. It is seen from Fig. 1 that this linear region extends to a coverage of about two monolayers. Above this linear region, both the low- and high-energy peaks tend to approach limiting values corresponding to infinite exposure, i.e. the xenon crystal surface in equilibrium with the xenon background pressure. The low- and high-energy peaks do however show quite different behavior with exposure to xenon gas.

The diminishing rate at which the high-energy peaks increased is the more predicted behavior and is indicative of the fact that the sticking probability is decreasing with increasing coverage. The change with exposure is not only dependent on the change in sticking probability, but also includes the effect of the incident beam exciting more xenon atoms as the coverage increases with fewer Auger electrons escaping because of their constant extinction distance λ_e. A calculation of the dependence of the Auger electron intensity in terms of the above fac-

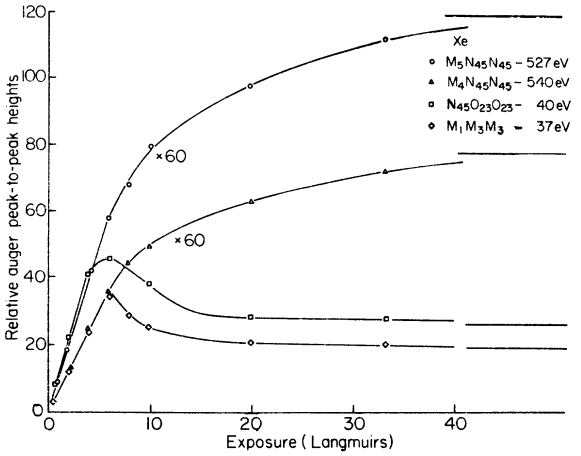

FIG. 1. Peak-to-peak heights of four xenon Auger electron peaks in the $dN(E)/dE$ vs E spectrum as a function of xenon exposure. The limiting values at very large exposures are indicated by the horizontal lines.

tors yields an exposure-coverage calibration valid beyond the linear region. This indicates that limiting values of the Auger signals correspond to a xenon coverage of 10–20 layers.[17] This result is in good agreement with the coverage determinations obtained from the extrapolated gas adsorption isotherms described previously.

The low-energy xenon-Auger-peak intensities, however, exhibit a different dependence on coverage in that they exhibited a maximum value at approximately 1.8 monolayers xenon coverage. This can be interpreted[17] in terms of the dependence of the iridium-Auger-peak intensities on xenon coverage resulting from the excitation of the low-energy xenon Auger transitions in the xenon-iridium interface region by iridium Auger electrons of sufficient ionization energy: 155, 163, and 173 eV. This secondary ionization initially increased the low-energy xenon Auger electron intensity. As the thickness of the xenon layer increases, however, the xenon Auger electrons created principally at the xenon-iridium boundary are increasingly damped. Such a behavior can be shown to produce a peak in the low-energy xenon Auger electron intensity data as a function of coverage.

B. Xenon Crystal Order

The two-dimensional order of the xenon crystals grown by vapor deposition was deduced from the diffraction spot sizes. In this analysis it was considered that the iridium substrate was free of imperfections, i.e., the iridium grain size was much larger that the coherence length of the incident electron beam (100–500 Å). This is realistic since the average grain size of carefully grown well-annealed films of fcc single crystals are typically 1 mm or more.[21] The difference in spot size between the xenon and iridium diffraction spots could therefore be used to measure the xenon crystal two-dimensional order.[22] Figure 2 shows a comparison of scans of the (00) spot intensities as a function of position in k space of a xenon crystal grown on a 1×5 Ir (100) surface and the 1×5 Ir (100) surface itself. The difference in half-height peak widths indicates that the xenon crystal surface consisted of grains with a typical size of approximately 450 Å in diameter. This grain size is the order of the incident beam coherence length and indicates that the surface disorder present at the grain boundaries is not likely to affect seriously the coherent scattering of the incident beam. The best-ordered xenon crystals were grown on the 1×5 Ir(100) and therefore all subsequent data are presented for this specific substrate.

C. Xenon Crystal Composition

The purity of the grown xenon crystals was monitored using glancing angle excitation high-sensitivity Auger electron spectroscopy.[23] The Auger spectrum for xenon is shown in Fig. 3. All peaks observed in the spectrum can be indexed as xenon Auger peaks with no ambiguity in identification with any possible impurity peaks. The absence of impurities observed at the Auger detection limit (better than 1% of a monolayer) could be due to electron-stimulated desorption (ESD).[24] The effect of this process on the detection of impurities adsorbed from the residual gas in the chamber was checked. It was concluded that the adsorption of impurity gas atoms on the xenon surface was negligible and hence did not influence the interpretation of the scattering measurements.

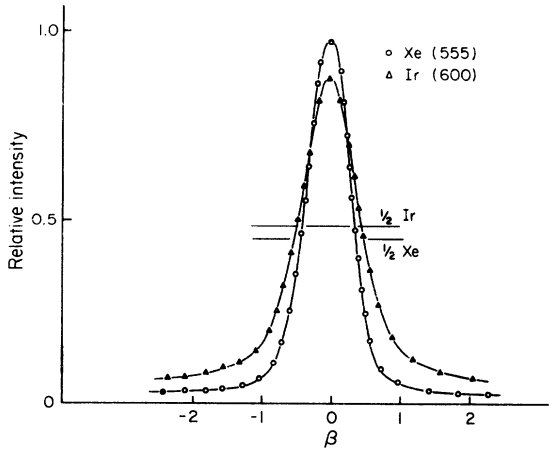

FIG. 2. Spot-photometer scans of the (00) beam in k space for iridium and xenon. Note the wider half-width for the xenon scan. The value β is the angle subtended as seen from the crystal.

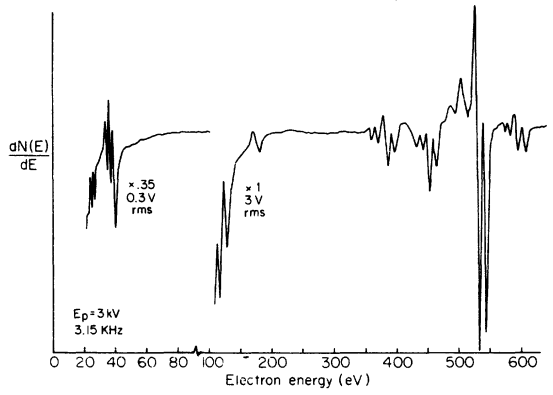

FIG. 3. Auger spectrum of crystalline xenon. All the observed peaks are documented xenon peaks.

IV. ENERGY DEPENDENCE OF LEED INTENSITY-ENERGY SPECTRA

Spectra of the elastically scattered intensity as a function of incident electron energy and angle were taken for the specularly reflected (00) beam and the nonspecular $(\bar{1}0)$, $(0\bar{1})$, $(\bar{1}1)$, and $(1\bar{1})$ beams in order to deduce information about the atomic structure of the xenon single-crystal films and to obtain information on the effect of energy and temperature on the mechanisms for electron scattering in xenon.

A. Intensity-Energy Spectra

The intensity-energy spectrum of the specularly reflected beam of xenon (111) is shown in Fig. 4. It should be noted that this spectrum is quite different from most LEED spectra[6] in that (a) there is one and only one peak for every expected Bragg reflection, (b) deviation from the Bragg positions after a correction for a constant inner potenital is very small (less than 1 eV), (c) the peaks have simple Lorenzian shapes, and (d) secondary structures are almost completely absent. The combination of these points defines a spectrum strongly characterized by kinematic scattering. This kind of scattering is very amenable to meaningful theoretical analysis in terms of the real parameters of the scattering system.

An interpretation for the observed kinematic scattering from crystalline xenon has been presented by Ignatjevs, Pendry, and Rhodin.[6] It is based on the proposal that because of the very large unit-cell size of crystalline xenon, which is about ten times larger than most metals, the elastic scattering is so weak that in conjunction with relatively strong inelastic scattering, multiple scattering events are so strongly reduced that the spectra are essentially dominated by kinematic scattering.

In addition to the above-noted conditions for stipulating the dominance of kinematic scattering, it should also be true that no splitting or erratic shifting of the Bragg peaks occur at higher angles of incidence. This condition is well satisfied for scattering from crystalline xenon, as shown in Fig. 5. Most of the Bragg peaks above approximately 30 eV remain relatively simple at most of the angles of incidence studied and only at 17.5° do lower-order fourth and fifth Bragg peaks show any splitting. The relative Bragg-peak intensities for xenon above 30 eV also generally behave as expected for a kinematic scatterer in that they reflect the dependence of the xenon scattering factor on scattering angle.[51] The intensity of the seventh-order Bragg peak (143 eV), however, changes quite markedly over the 5–17.5° range of incidence angle. This is attributed to the possibility that a very small multiple scattering resonance may be present in the 140-eV energy region. The overall behavior of the (00) beam intensity-energy spectra as a function of angle of incidence further strengthens the assumed kinematic nature of the electron scattering.

The intensity-energy spectra of the first-order nonspecular beams have also been measured. They show the same highly kinematic behavior as stated above for the specularly reflected beam. Spectra of the $(\bar{1}1)$, $(\bar{1}0)$, and $(0\bar{1})$ beams at normal incidence are shown for comparison in Fig. 6. It is seen that the spectra are essentially identical, indicating minimal extraneous magnetic field effects on the electron beam. The structures in the spectra are easily and unambiguously identifiable as

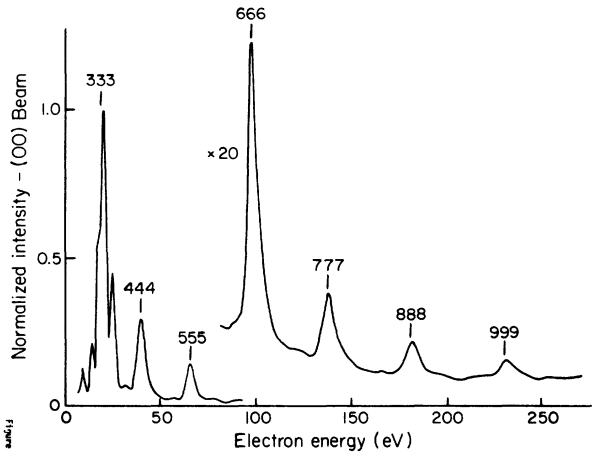

FIG. 4. Xenon (111) intensity-energy spectrum of the (00) beam at 6° from normal incidence and 58 °K. The Bragg-peak positions are noted after a constant 8-eV inner-potential correction. The spectrum is corrected for contact potential difference by a constant 4-eV shift to higher energies.

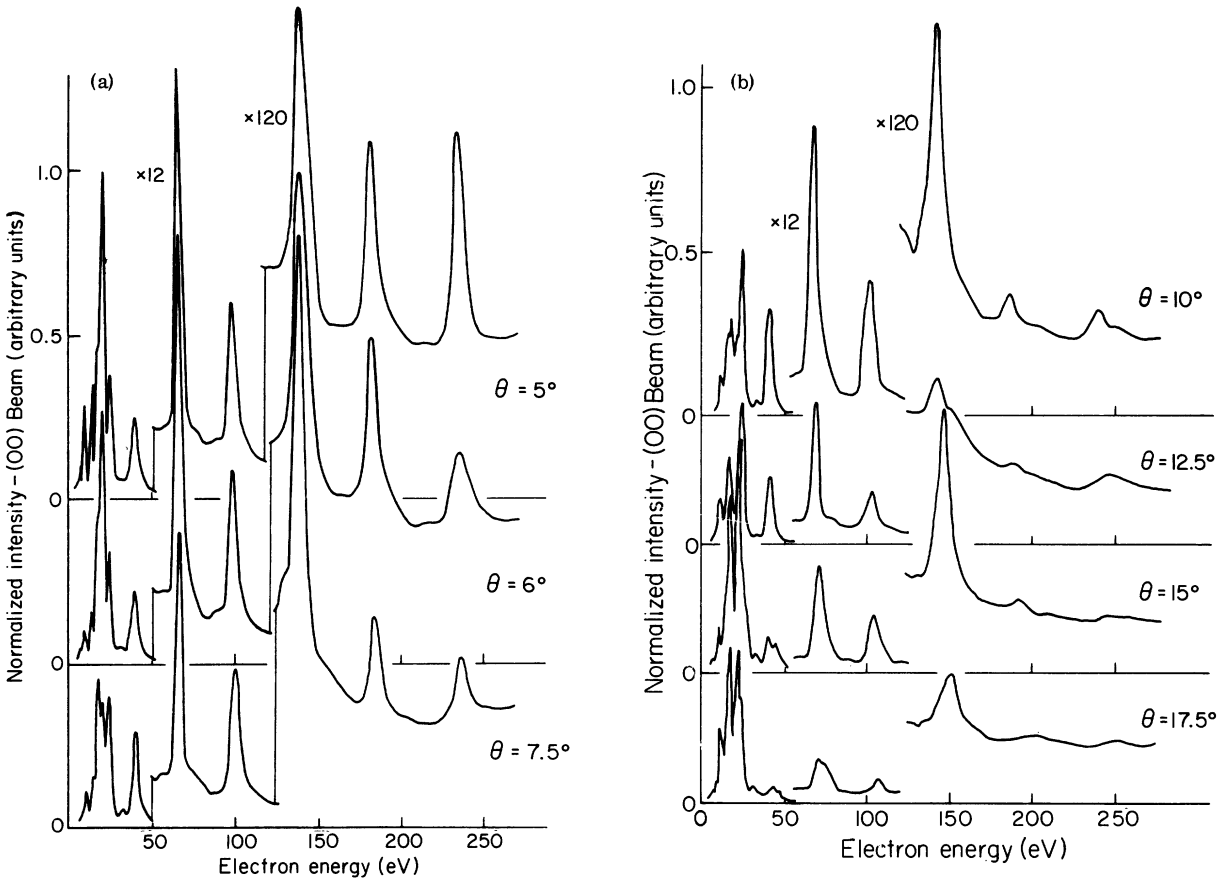

FIG. 5. Xenon intensity-energy spectra of the (00) beam over a range of the angle of incidence at 58 °K. The spectra are shifted 4 eV to higher energies to correct for contact potential difference.

Bragg scattering with little or no additional structure above 40 eV. The main differences in the spectra occur in the 40-eV region in the form of peak shifts among spectra, and in the 120–140-eV region where noticeable decreases in the (775) and (886) Bragg peaks are observed in the $(\bar{1}0)$ and $(0\bar{1})$ spectra. It should be noted that this decrease in intensity in the 140-eV region is probably due to the change of azimuthal angle between the $(\bar{1}0)$, $(0\bar{1})$ and the $(\bar{1}1)$, $(1\bar{1})$ beams and may be attributed to a minimal amount of multiple scattering. This region of nonkinematiclike behavior curiously falls in the same energy range as that of the observed nonkinematic behavior in the specular beam. The double-peak nature of the nonspecular spectra is due to the possibility that the fcc lattice may be built up on the first (111)-type layer of xenon in two different ways with consequential mixing of the (nmm) and (nnm) families of Bragg peaks in each lowest-order nonspecular beam.

Nonspecular beam spectra were also taken at different angles of incidence of the electron beam where the angle of incidence was varied along a nonsymmetry direction, $\phi = -22°$, of the (111) surface. Figure 7 shows the large variation of peak intensities upon changing the angle of incidence from normal incidence to 5°. The peaks however do not split and no new peaks are observed up to a 15° angle of incidence. It should be noted that in measuring nonspecular beam spectra, the Bragg scattering angle θ_{B_g} is different for each peak in the spectra. The change in the nonspecular Bragg-peak intensities with changing incidence angle may therefore be a consequence of changing Bragg scattering angle. Figure 8 shows the variation of the intensity of the $(1\bar{1})$ beam with the angle of incidence. The Bragg scattering angle is noted above each Bragg peak. It is seen that there is a general trend of decreasing peak intensities with increasing scattering angle. This trend is consistent with the behavior of the xenon scattering factor with angle.[51] There is again, however, some irregular behavior in the 120–140-eV region, probably because of some multiple scattering. In addition, it is observed that for most peaks in the $\theta = 10°$ scan, the scattering angles are all within ~ 1.5°, i.e., the

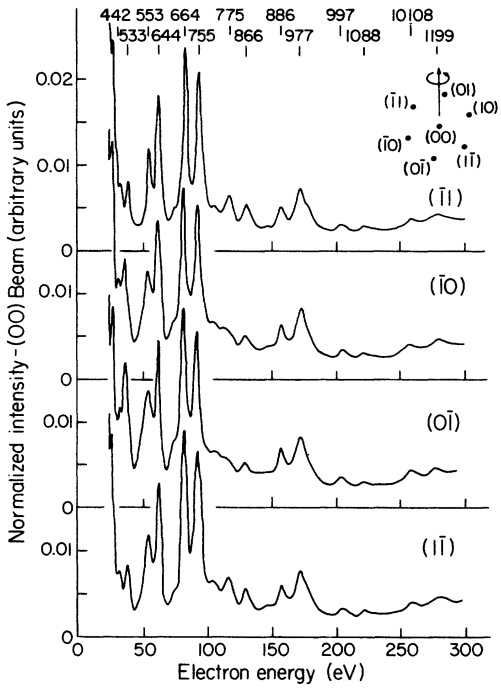

FIG. 6. Xenon intensity-energy spectra of the $(\bar{1}1)$, $(0\bar{1})$, $(\bar{1}0)$, and $(\bar{1}1)$ beams at normal incidence and 60 °K with the arbitrary normalized intensity defined as fractions of the (333) Bragg-peak intensity in the (00) beam at 5° incidence. The Bragg-peak positions are noted after including an 8-eV inner-potential correction. The spectra are corrected for contact potential difference by a constant 4-eV shift to higher energies.

spectrum may be roughly considered as being taken at a constant scattering angle. The systematically decreasing character of the intensities with energy in this spectrum is a direct result of the general highly kinematic behavior of electron scattering from xenon.

B. Xenon Inner Potential

The xenon lattice parameter was determined from Bragg-peak positions in the (00) beam spectra. The derived result of $a_0 = 6.17 \pm 0.01$ Å at 55 °K is in excellent agreement with the x-ray determination of $a_0 = 6.173$ Å.[25] An inner-potential correction was, however, needed to correlate experimental peak positions with values calculated using a temperature-dependent lattice parameter. An additional correction for the contact potential difference (CPD) between the xenon crystal and the electron-gun filament was included. A CPD of 4 eV was deduced from xenon band-structure calculations[26] and from the work function of the electron-gun cathode. Consequently all intensity-energy spectra are corrected for the CPD by a constant 4-eV shift to higher energies. The variations of the xenon inner-potential correction as a function of electron energy is shown in Fig. 9 for both the specular and nonspecular beams. It is observed that the inner potential has a peculiar dip at 140 eV. It was previously pointed out that peak intensity variations in this same energy region may be due to the presence of a relatively small amount of multiple scattering. It is quite possible that such multiple scattering contributions could shift Bragg peaks and result in the observed fluctuation in the inner potential.

Theoretical predictions of the inner potential in low-energy electron scattering[5,27] do not agree with the character of the xenon experimental observations. There is reason to believe that the differences are probably due more to the approximations in the analyses than to the interpretation of the experimental data.

C. Bragg-Peak Half-Widths—Electron Damping in Xenon

In a simple scattering system, the Bragg-peak widths are determined essentially by the electron lifetime broadening. Hence the inelastic scattering potential V_i can be related to the Bragg-peak half-width ΔE by

$$V_i = \tfrac{1}{2}\Delta E \ . \qquad (1)$$

For xenon, a highly kinematic scattering system, Eq. (1) can be used to determine the xenon inelas-

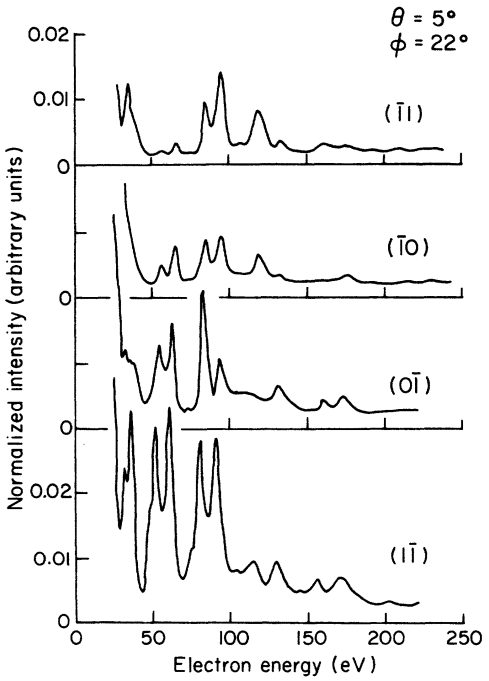

FIG. 7. Xenon intensity-energy spectra of the (11), $(0\bar{1})$, $(\bar{1}0)$, and $(\bar{1}1)$ beams at 5° from normal incidence and 60 °K. The spectra are corrected for contact potential difference.

tic scattering for the observed peak widths. Figure 10 shows that the experimental peak widths increase with increasing electron energy for xenon. The electron penetration depth or extinction distance λ_e can be derived from the inelastic scattering potential according to the expression

$$\lambda_e = \frac{[(\hbar^2/2m)E]^{1/2}}{V_i} . \quad (2)$$

Using the observed Bragg-peak widths to determine the inelastic scattering potential however leads to the implausible conclusion that the electron penetration depth is essentially constant with electron energy up to 500 eV. It is concluded therefore that the peak widths at the higher energies above 200 eV are not a simple reflection of the xenon inelastic scattering potential V_i.

The magnitude of the xenon inelastic scattering potential corresponding to certain specific electron energies was investigated independently by monitoring the iridium Auger electron damping in xenon. The decrease in intensity of two strong iridium Auger peaks was monitored as a function of xenon coverage. This yielded electron extinction distances of approximately 5.5 Å at 55 eV and 11.5 Å at 163 eV. The reliability of these results depends on the assumption that the xenon films are formed in uniform layers, e.g., the xenon atoms do not cluster upon adsorption, but spread themselves evenly in every layer. This has been shown to be the case for inert-gas atoms adsorbed on metallic substrates,[16] hence it is concluded that the damping interpretations deduced for the measurement of the penetration of iridium electrons through the xenon films are valid. The xenon inelastic scattering potential obtained from the damping measurements was 2.6 ± 0.3 eV at 55 eV, and 2.0 ± 0.3 eV at 163 eV. These values of the scattering potential are also shown in Fig. 10. It is seen that the inelastic scattering potential obtained from the Bragg-peak half-widths compares well with those deduced from the iridium Auger electron damping at electron energies up to approximately 200 eV. The Auger electron damping measurements are a more reli-

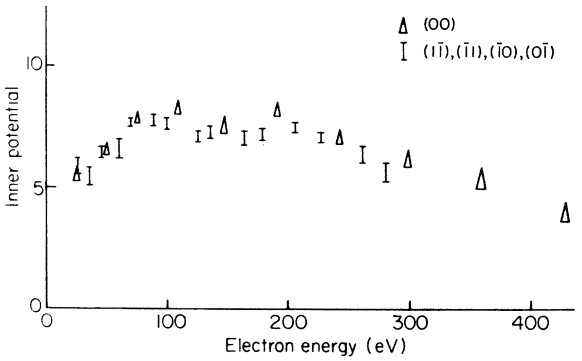

FIG. 9. Energy dependence of the inner potential for the specular and nonspecular beams.

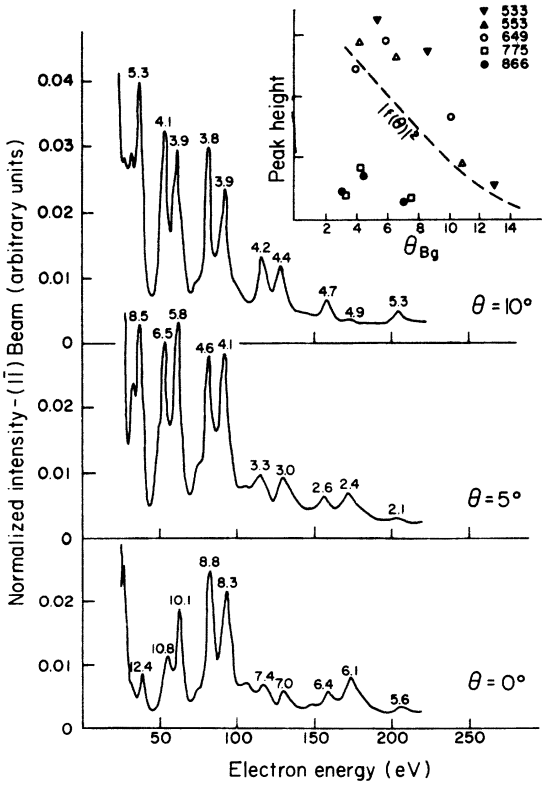

FIG. 8. Xenon intensity-energy spectra for the (1$\bar{1}$) beam at 0°, 5°, and 10° from normal incidence. The effective scattering angle θ_{Bg} is noted above each peak at each angle of incidence. The behavior of the peak intensities with scattering angle is compared with that of the scattering factor with scattering angle.

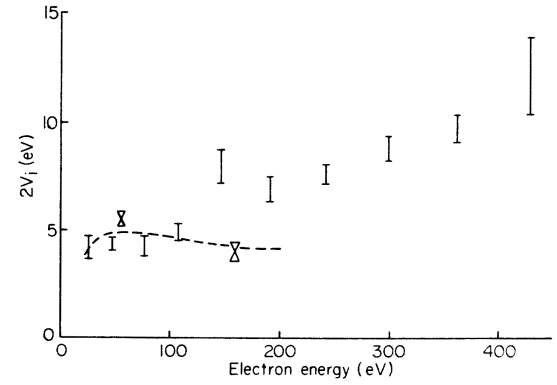

FIG. 10. Xenon inelastic scattering potential determined from the Bragg-peak half-widths (bars), from iridium Auger electron damping (crosses), and the trend of the dependence as suggested by Lundqvist (Ref. 5) (dashed line).

able indication of λ_e than the half-width measurements, since the former directly measure the xenon inelastic scattering potential. The divergence of the Bragg-peak half-width data at high energies can be due to the occurrence of some multiple scattering. It is sufficient to note here that no definite assertion as to the role of multiple scattering in the high-energy range can be made until a complete theoretical calculation based on the multiple scattering formalism is made for xenon.

V. TEMPERATURE DEPENDENCE OF LEED INTENSITY–ENERGY SPECTRA

A. Lattice Vibrations–Debye-Waller Factor

In addition to the variation of the scattered electron intensity with energy, a systematic dependence of the scattered intensity on temperature is also observed. This temperature effect can be expressed for the (00) beam in the kinematic scattering formalism, where the scattered intensity in the presence of thermal vibration of the lattice is

$$\langle I\rangle = I_{\mathrm{Bg}} e^{-2M}(1 + Q^2\langle u_Z^2\rangle + \tfrac{1}{2}Q^4\langle u_Z^2\rangle + \cdots) \ , \qquad (3)$$

where

$$M = \tfrac{1}{2}Q^2\langle u_Z^2\rangle \ , \qquad (4)$$

and

$$Q = |\vec{k}_Z - \vec{k}_Z'| \ . \qquad (5)$$

The angular brackets $\langle\ \rangle$ denote a thermal average and $\langle u_Z^2\rangle$ is the mean-square vibrational amplitude of the atoms in the z direction (normal to the surface).

The first term in Eq. (3) is the Bragg-scattered intensity term modified by e^{-2M}. The second term is the contribution to the scattered intensity from one-phonon scattering processes. The third term is the contribution to the intensity from two-phonon scattering processes, etc.

Focussing attention on the first term of Eq. (3), one sees that the intensities of the Bragg peaks are modified by a factor of e^{-2M}, with the lost intensity redistributing itself through k space among one-phonon, two-phonon, and multiphonon scattering contributions. The temperature dependence of the first term is therefore that of the exponent M, or the atomic mean-square vibration amplitudes. The term $\langle u_Z^2\rangle$ can be easily evaluated in the high-temperature limit $T > \Theta_D/2\pi$, [28]

$$\langle u_Z^2\rangle = 3\hbar^2 T/m_a k_b \Theta_D^2 \ , \qquad (6)$$

where m_a is the mass of the atom and Θ_D is the Debye temperature. The first term in Eq. (3) (the modified Bragg-scattered term) can therefore be written as

$$\log_{10} I = -\frac{10.5E\sin^2\theta}{m_a/m_e k_b \Theta_D^2}\, T + \mathrm{const} \ , \qquad (7)$$

where E, the energy of the electron, is

$$E = (\hbar^2/2m_e)|\vec{k}|^2 \qquad (8)$$

and θ is the angle of incidence of the electron beam.

From Eq. (7) it is seen that for a kinematic scattering system, the logarithm of the intensity decreases with increasing temperature and with increasing electron energy and is inversely proportional to the square of the Debye temperature of the material. Since low-energy-electron scattering probes the surface layers of a material, the scattered intensity will be a function of the surface Debye temperature. Therefore, the surface or effective Debye temperature can be obtained from observations of the logarithmic behavior of the Bragg-peak intensities with temperature. For a kinematical scattering system, it is also possible to derive the mean-square vibrational amplitudes per atomic layer of the crystal from analysis of these data. Such measurements provide a unique opportunity to obtain information on the force laws and interaction potential specific to the surface layers of the crystal.

There have been many attempts to interpret temperature effects at surfaces of solid crystals using LEED since the initial work of Germer and MacRae.[29] Webb and co-workers[30–33] made careful measurements on the silver and nickel systems. Lyon and Somorjai[34] observed thermal scattering in platinum. Tabor, Wilson, and Bastow[35] have studied the chromium and molybdenum systems. Quinto, Holland, and Robertson[36] worked on aluminum and others[37–42] have studied copper, palladium, lead, niobium, zinc, bismuth, and iridium. All of these studies were done on metallic crystals. The surface Debye-temperatures were computed assuming a kinematic scattering model. In addition, in almost all cases the rather questionable assumption was made that only the top surface layer exhibited a Debye temperature (or mean-square vibration amplitude) different from that of the bulk.

The former assumption appears doubtful since multiple scattering is known to make a very strong contribution to both peak positions and intensities in the LEED spectra of metallic systems. Some recent LEED calculations[43,44] of effective Debye temperatures for metallic surfaces based on dynamical models have shown a logarithmic dependence of intensity with temperature. However, the significance of these calculations is not settled. There appears to be no defined basis at this time to determine the limits of valid applicability of the kinematic analysis of the temperature dependence for highly dynamic scattering systems. With reference to the latter assumption, although an effective surface Debye temperature can be readily obtained from the measured temperature depen-

dence of the intensity of a given peak, the assumption that it can be simply related to the mean-square vibration amplitude of a single surface layer is questionable. Model calculations have shown,[7-9,45] and it is physically more realistic to consider, that there is a gradual and discrete variation of the atomic mean-square vibration amplitudes from the top surface layer to the bulk. These considerations are developed more quantitatively for noble-gas crystals in the following paper.[51]

B. Intensity-Energy Spectra as a Function of Temperature

Figure 11 shows a series of intensity-energy spectra for the (00) beam of xenon (111) taken as a function of temperature. The most consistent data were obtained by growing the xenon single crystals at approximately 55 °K, heating the crystals to approximately 73 °K to anneal them and then first decreasing and then increasing the temperature to get successive intensity-energy spectra of the (00) beam at various intermediate temperatures. The annealing was necessary to achieve well-ordered single-crystal films, and often produced a 10–15% increase of the peak intensities. The total time needed for a "run," i.e., the time

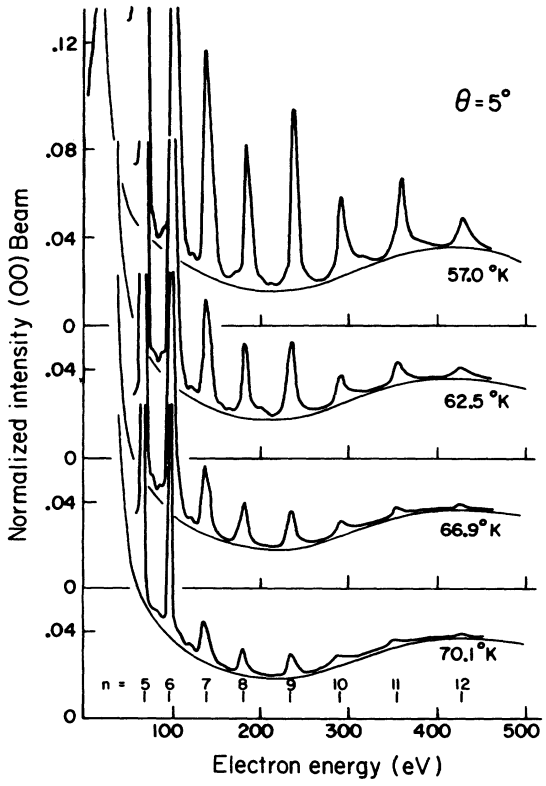

FIG. 11. Xenon (111) intensity-energy spectra of the (00) beam as a function of temperature taken at 5° away from normal incidence. The background-intensity corrections are shown as solid lines.

interval needed to go from ~73 to ~55 °K, including taking intensity-energy spectra at usually five different temperatures over the range, was about 1.5 h. The crystal was typically held at each specific temperature for between 5 and 10 min before the spectra were taken. On most occasions, two or three different runs would be made on each crystal, (run 1) temperature decreasing, (run 2) temperature increasing, and (run 3) temperature decreasing. The Bragg-peak intensities for these runs for any one xenon crystal matched to within 3%. Since it has been observed that peak intensities can change by up to 20% for surface contaminations of as low as 0.1 monolayers,[46] the observed maximum 3% variation further supports the Auger spectroscopic observation that there was negligible adsorption of impurities on the xenon surface over the 3–4 h period of investigation.

Before Bragg-peak intensities could be determined from the intensity-energy spectra, a systematic subtraction of the background intensity had to be undertaken. The background intensity is defined as that intensity which is dependent only on the scattering angle. It is due mainly to two factors: (a) intensity scattered from noncoherently scattering structures, and (b) intensity scattered from the excitation of phonons. The background intensity was obtained by taking scans of the elastically scattered intensity as a function of scattering angle 2θ for several angles of incidence, as proposed by Lagally and Webb.[33] The resulting background-intensity corrections are shown as smooth lines in Fig. 11.

It must be realized that in addition to taking into consideration the background-intensity contribution partially consisting of multiphonon scattered intensity, the intensity contributions from one-, two-, etc., phonon processes should also be taken into account. An effort was made to eliminate such contributions from the measurement by stopping down the aperture of the spot photometer used to photometrically record the intensity data to 0.8° as subtended from the crystal. As a result, intensity due to phonon scattering for phonons of $|\vec{q}| \geq B_g/40$ at 70 eV, where B_g is the Brillouin-zone boundary, was not measured. Of the remaining possible small $|\vec{q}|$ phonon scattered intensity, single-phonon scattering processes will be most dominant.[17] These will, therefore, be the primary possible contributions to the collected Bragg-peak intensity. It is observed, however, that single contributions are not evident below an acceptance angle of ~2° for the xenon (444) Bragg peak and ~0.8 to 1.0° for the (888) Bragg peak.[17] Such contributions, which do not have a simple logarithmic behavior with temperature, will therefore not be integrated into the Bragg-peak intensities, at least up to the eighth-order Bragg peaks and hence will

not affect the measured effective Debye temperature.

The Bragg-peak intensities needed for the $\log_{10}I$ vs T plot and measured under the above conditons can therefore be directly obtained from the spectra illustrated in Fig. 11 after subtraction of the background-intensity contributions. A total of 39 peak intensity vs temperature points were taken for the fourth through ninth Bragg peaks and ten points were taken for the tenth through twelfth Bragg peaks over the temperature range 55–75 °K. These data were taken for five specific xenon crystals and a total of ten separate runs. These data are summarized in Fig. 12. The amount of scatter in the points is due primarily to measurements from several different crystals. This was needed, however, to achieve a full representation of the temperature dependence of the scattered intensities over the complete 55–75 °K temperature range. Although this 20 °K temperature range is rather small on an absolute scale, it corresponds to a temperature variation of approximately 30% of the xenon bulk Debye temperature at absolute zero temperature and is characterized by minimum Bragg-peak intensity variations of 40%.

Least-squares-fit straight lines were fitted to the $\log_{10}I$ vs T points. The values of the effective

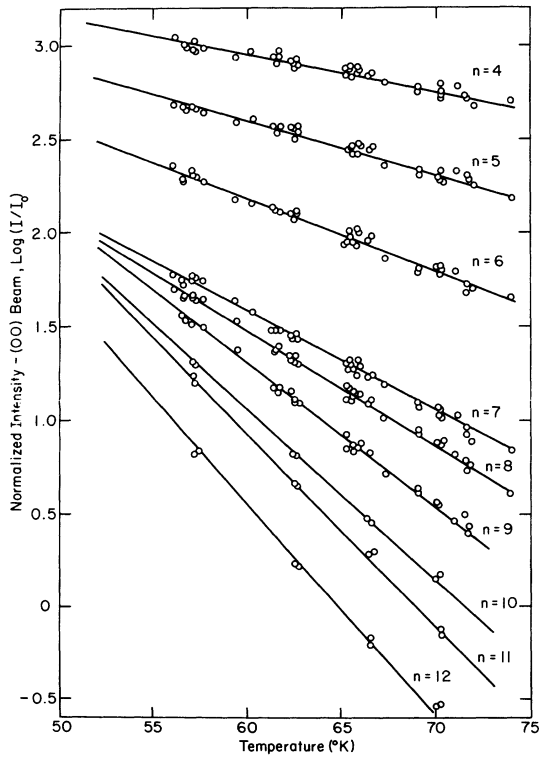

FIG. 12. Least-squares-fit lines to the data of the Bragg-peak intensities as a function of temperature.

TABLE II. Experimentally derived effective Debye temperatures for xenon as a function of Bragg-peak order number.

n-Bragg-peak number	$\Theta_{D\,\mathrm{eff}}$(Expt.)(°K)
4	34.2 ± 1.1
5	35.0 ± 0.8
6	36.1 ± 0.6
7	38.1 ± 0.6
8	39.6 ± 0.5
9	40.4 ± 0.6
10	41.2 ± 1.1
11	42.1 ± 0.9
12	43.7 ± 1.2

Debye temperatures and the error in their determination, given in Table II, were derived from the slopes and the mean deviation of the slopes of the constructed straight lines. Straight lines were fitted to the data on the assumption that the xenon effective Debye temperatures would not change drastically with temperature over the temperature range used. The likelihood of this possible temperature dependence being significant was, however, investigated, with the result that a maximum 4% change of the effective Debye temperature with temperature was observed. This minimal variation justifies the practice of fitting straight lines to the points over the complete temperature range.

The energy dependence of the determined effective Debye temperature is more readily seen in Fig. 13. It should be noticed that the effective Debye temperature is smaller at the lower energies. This indicates that the outer layers vibrate with larger mean-square vibration amplitudes than inner layers and that at low energies the incident electrons sample mainly top surface layers. It should also be noticed that the effective

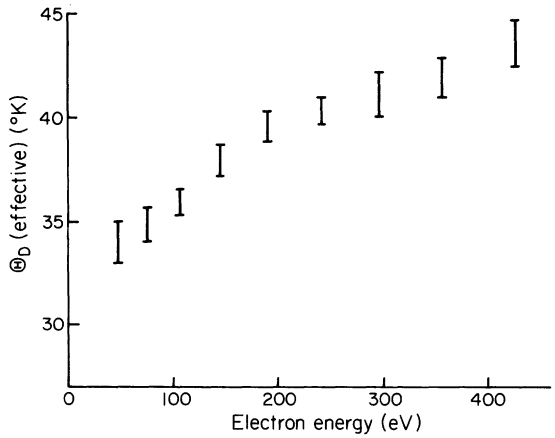

FIG. 13. Effective Debye temperature for xenon as a function of energy determined from the slopes of the straight lines of Fig. 12.

Debye temperature levels off at higher energies. The limiting value of ~43 °K, however, is below the heat capacity deduced bulk Debye-temperature of ~56 °K for the temperature range used.[47] This difference is not unexpected since diffraction measurements of the bulk Debye temperature and specific heat measurements do not sample the same types of modes in the phonon density of states and therefore would not necessarily be expected to yield equivalent values for the bulk Debye temperature.[48] There are, however, no equivalent values of the xenon bulk Debye temperature available for comparison derived from diffraction measurements.

C. Xenon Thermal Expansion

An additional interesting point in the behavior of the intensity-energy spectra with temperature is the effect of temperature on the Bragg-peak positions. Since the xenon spectra are highly kinematic in character, the temperature dependence of the displacement of the Bragg peaks can be readily interpreted within the kinematic framework. Hence, shifts in the Bragg peak positions with temperature are simply related to changes in the xenon (111) interlayer d spacing, that is, changes due to the thermal expansion of the surface layers.

In a kinematic scattering system, the thermal expansion coefficient is defined by

$$\alpha = -\frac{1}{2E_{Bg}}\frac{dE_{Bg}}{dT} \quad , \tag{9}$$

where E_{Bg} is the Bragg energy. Plots of the Bragg-peak energy as a function of temperature were taken to obtain the variation of α with energy (Fig. 14). It is seen in Fig. 14 that α is essentially equal to the bulk value[25] at energies greater than approximately 350 eV, and that it increases smoothly to about four to five times the bulk value at 20–40 eV. The large increase at the low energies indicates that the uppermost layers of the xenon crystal have thermal expansion coefficients significantly larger than that of the bulk. However, the value associated with the low-energy (20 eV) electrons is an average coefficient of expansion representative of all layers sampled. Because of the decreased penetration depth λ_e at the lower energies, the 20-eV electrons sample the uppermost layers more heavily than the higher-energy electrons. The α of the top layer has to be deconvoluted from the contributions of the rest of the layers to the observed coefficient of expansion. It can be assumed however, that the observed α at a certain energy corresponding to a specific penetration depth is a lower bound on the coefficient of expansion of the layer corresponding to that depth.

For example, for 23-eV electrons (from Sec. IV C) $\lambda_e \simeq 1.2$ layers, therefore the coefficient of expansion observed in the direction normal to the surface at 23 eV can be considered to be the lower bound on the value of α for the top surface layer. Thus,

$$\frac{\alpha_{\text{surface layer}}}{\alpha_{\text{bulk}}} \simeq 4\text{–}5 \quad .$$

Recent calculations[49,50] of the surface thermal expansion coefficient, assuming α proportional to the specific heat with the surface atoms as simple harmonic oscillators, have shown

$$\frac{\alpha_{\text{surface region}}}{\alpha_{\text{bulk}}} \simeq 2\text{–}2.5 \quad .$$

This is a factor of 2, if not more, lower than the observed value and may be due to some contributions that may be overlooked in the computational model.

Although the above observations indicate that the surface layers expand more than the bulk layers, they do not indicate whether the surface layer (or layers) may be initially expanded or contracted with respect to the bulk. The measurement of the xenon inner-potential correction does, however, clarify this point. Since the scattering from xenon is highly kinematic in nature, the assumption that there are very few or essentially no multiple scattering contributions to the xenon Bragg-peak positions is quite realistic. The measured inner-potential correction is therefore a function of the actual xenon inner potential and possible contributions to peak positions from surface-layer expansion.

The xenon inner-potential correction shown in Fig. 9 indicates a decreasing value at low energies. This is contrary to model inner-potential calculations,[5] but is consistent with a proposed surface-layer expansion of the xenon crystal. The decreasing inner-potential correction indicates that

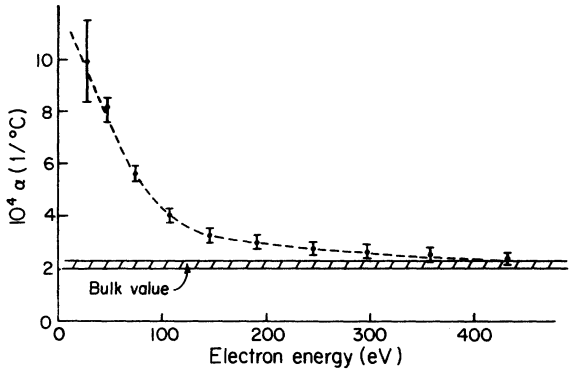

FIG. 14. Coefficient of thermal expansion α as derived from the linear behavior of the Bragg-peak positions as a function of temperature.

the lattice parameter normal to the surface used to determine the correction is too small at the low energies. Thus the surface layers of the xenon crystal, sampled more heavily by the electrons in the low-energy range because of decreased penetration, are expanded more than the bulk.

The above suggestion was quantitatively checked by monitoring the temperature dependence of the inner-potential correction. It is seen from Fig. 15 that at above approximately 200 eV, the inner-potential correction is essentially temperature independent. Since the observed thermal expansion at these energies is that of the bulk, this was corrected by using a temperature-dependent bulk lattice constant to determine the inner-potential correction. The temperature-independent behavior, therefore, indicates a temperature-independent inner-potential contribution to the xenon inner-potential corrections. At the low energies, however, a lower value for the inner-potential correction is observed at 56 °K than at 65 °K. This behavior is consistent with the previous thermal expansion measurements. At 23 eV, Fig. 15 indicates a thermal expansion of approximately 1.2% for the 65 °K data over that at 56 °K. For the same energy and temperature interval, the thermal expansion data of Fig. 14 yield a 1% expansion. This correlation indicates that the xenon Bragg-peak positions at low energies are particularly sensitive to the spacing of the surface layers. The low-energy deviation of the inner-potential correction from the near constant mid-energy-range of 8 eV is therefore taken to be due primarily to relaxation of the xenon crystal surface layers. This relaxation is in the form of a surface expansion of about 5.7% as measured at 23 eV and 2% at 45 eV. Again, because of the depth averaging of the electrons, the 5.7% expansion measured at 23 eV is at least a lower bound on the degree of relaxation of the top surface layer. Model calculations[8] of the surface-layer relaxation predicting a 4% top surface-layer expansion are in good agreement with these observations.

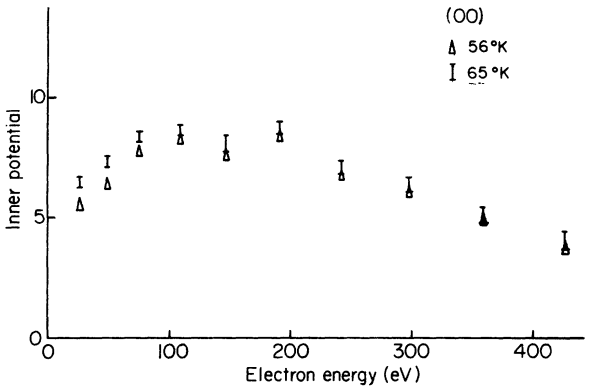

FIG. 15. Temperature dependence of the xenon inner-potential showing (for lower energies) a higher inner-potential correction at higher temperatures indicative of surface-layer expansion.

VI. DISCUSSION AND CONCLUSION

The temperature and energy dependence of low-energy electron scattering from a xenon single-crystal surface is presented here. The xenon crystals were formed with a (111) surface orientation and were of very good order and purity. The outstanding feature of the surfaces from an experimental viewpoint is that kinematic scattering is the dominant scattering process for low-energy electrons. This feature makes it possible to obtain critical observation and analysis of electron scattering properties in the kinematic scattering formalism. From this viewpoint, analyses of the xenon effective Debye temperature and the thermal expansion of xenon are presented.

A more complete analysis of electron scattering based on the kinematic formalism is presented in the following paper,[51] which includes the comparison of the xenon effective Debye temperature to surface atom mean-square vibration amplitude calculations previously predicted by Allen and DeWette[7,9] and by Allen, DeWette, and Rahman[8] and the extraction of electron damping in solid xenon.

In conclusion, single-crystal xenon has been found to provide a unique kinematic scattering system for low-energy electron scattering. For such a system, because of its amenability to analysis, a more complete interpretation of the surface lattice dynamics at the surface of inert-gas crystals can be achieved.

ACKNOWLEDGMENTS

The benefit of stimulating discussion with S. Y. Tong through various stages of this study is gratefully acknowledged. The initial contributions of A. V. Jones to experimental design and construction is appreciated. Helpful discussions with J. B. Pendry, B. Lundqvist, and D. L. Adams are also acknowledged. Finally, experimental assistance from J. Starbuck and B. Hutchins is also noted with appreciation.

*Principal research support by the National Science Foundation under Grant No. GH-31909 and supplementary support from the Cornell Materials Science Center are acknowledged.

†Present address: Department of Materials Science, State University of New York at Stony Brook, Stony Brook, N.Y. 11790

[1]C. J. Davisson and L. H. Germer, Phys. Rev. **30**, 705 (1927).
[2]R. M. Tait, S. Y. Tong, and T. N. Rhodin, Phys. Rev. Lett. **28**, 553 (1972).
[3]D. W. Jepsen, P. M. Marcus, and F. Jona, Phys. Rev. B

5, 3933 (1972).
[4]J. B. Pendry, Phys. Rev. Letters 27, 856 (1971).
[5]B. I. Lundqvist, Phys. Status Solidi 32, 273 (1969).
[6]A. Ignatjevs, J. B. Pendry, and T. N. Rhodin, Phys. Rev. Lett. 26, 189 (1971).
[7]R. E. Allen and F. W. DeWette, Phys. Rev. 179, 873 (1969).
[8]R. E. Allen, F. W. DeWette, and A. Rahman, Phys. Rev. 179, 887 (1969).
[9]R. E. Allen and F. W. DeWette, Phys. Rev. 188, 1320 (1969).
[10]J. A. Venables and D. J. Ball, J. Cryst. Growth 3, 180 (1968).
[11]H. M. Kramer, G. L. Price, and J. A. Venables, in Proceedings of the Twenty-Fifth Anniversary Meeting of Emag. Institute of Physics, 1971 (unpublished).
[12]R. F. Steiger, J. M. Morabito, Jr., G. A. Somorjai, and R. H. Muller, Surf. Sci. 14, 279 (1969).
[13]P. W. Palmberg, Surf. Sci. 25, 598 (1970).
[14]J. M. Dickey, H. H. Farrell, and M. Strongin, Surf. Sci. 23, 448 (1970).
[15]H. H. Farrell, M. Strongin, and J. M. Dickey, Phys. Rev. B 6, 4703 (1972); Phys. Rev. B 6, 4711 (1972).
[16]A. Ignatiev, A. V. Jones, and T. N. Rhodin, Surf. Sci. 30, 573 (1972).
[17]A. Ignatiev, Ph.D. thesis (Cornell University, 1972) (unpublished).
[18]F. Ricca and A. Bellardo, Z. Phys. Chem. (Leipz.) 52, 318 (1967).
[19]F. Ricca, R. Medana and A. Bellardo, Z. Phys. Chem. (Leipz.) 52, 276 (1967).
[20]S. Dushman, *Scientific Foundations of Vacuum Techniques* (Wiley, New York, 1962).
[21]F. W. Young, J. Appl. Phys. 35, 1917 (1968).
[22]D. L. Adams and L. H. Germer, Surf. Sci. 26, 109 (1971).
[23]A. Ignatiev and T. N. Rhodin, Amer. Lab. 4(11), 8 (1972).
[24]T. E. Madey and J. T. Yates, J. Vac. Sci. Technol. 8, 525 (1971).
[25]D. R. Sears and H. P. Klug, J. Chem. Phys. 37, 3002 (1962).
[26]U. Rossler, Phys. Status Solidi 42, 345 (1970).
[27]J. B. Pendry, J. Phys. C 2, 1215 (1969).
[28]J. M. Ziman, *Principles of the Theory of Solids* (Cambridge U. P., Cambridge, England, 1969).
[29]L. H. Germer and A. U. MacRae, Phys. Rev. Lett. 8, 489 (1962).
[30]E. R. Jones, J. T. McKinney, and M. B. Webb, Phys. Rev. 151, 476 (1966).
[31]J. T. McKinney, E. R. Jones, and M. B. Webb, Phys. Rev. 160, 523 (1967).
[32]R. F. Barnes, M. G. Lagally, and M. B. Webb, Phys. Rev. 171, 627 (1968).
[33]M. G. Lagally and M. B. Webb, in *The Structure and Chemistry of Solid Surfaces*, edited by G. A. Somorjai (Wiley, New York, 1969).
[34]H. B. Lyon and G. A. Somorjai, J. Chem. Phys. 44, 3707 (1966).
[35]D. Tabor, J. M. Wilson, and T. J. Bastow, 20, 471 (1971).
[36]J. C. Quinto, B. W. Holland, and W. D. Robertson, Surf. Sci. 32, 139 (1972).
[37]S. Andersson and B. Kasemo, Solid State Commun. 8, 1885 (1970).
[38]J. M. Baker, Ph.D. thesis (Cornell University, 1970) (unpublished).
[39]R. M. Goodman, Ph.D. thesis (University of California, Berkeley, 1969) (unpublished).
[40]R. J. Reid, Surf. Sci. 29, 623 (1972).
[41]R. M. Goodman, H. H. Farrell, and G. A. Somorjai, J. Chem. Phys. 48, 1046 (1968).
[42]D. Tabor and J. Wilson, Surf. Sci. 20, 203 (1970).
[43]F. Jona, D. W. Jepsen, and P. M. Marcus, Lecture Notes, Sixth LEED Seminar, Washington, D. C., 1972 (unpublished).
[44]G. E. Laramore, Phys. Rev. B 6, 1097 (1972).
[45]B. C. Clark, R. Herman, and R. F. Wallis, Phys. Rev. 139, A860 (1965).
[46]F. Jona, Surf. Sci. 8, 478 (1967).
[47]V. G. Manzelli, V. G. Gavrilico, and E. I. Votovich, Fiz. Tverd. Tela 9, 1483 (1967) [Sov. Phys.-Solid State 9, 1157 (1967)].
[48]B. W. Batterman and D. R. Chipman, Phys. Rev. 127, 690 (1963).
[49]R. E. Allen, J. Vac. Sci. Technol. 9, 934 (1972).
[50]J. M. Wilson and T. J. Bastow, Surf. Sci. 26, 461 (1971).
[51]S. Y. Tong, T. N. Rhodin, and A. Ignatiev, following paper, Phys. Rev. B 8, 906 (1973).

PHYSICAL REVIEW B VOLUME 8, NUMBER 2 15 JULY 1973

Layer-Dependent Surface Mean-Square Vibration Amplitudes by Low-Energy-Electron Diffraction*

S. Y. Tong,† T. N. Rhodin, and A. Ignatiev‡
School of Applied and Engineering Physics, Cornell University, Ithaca, New York 14850
(Received 5 January 1973)

The surface-vibration properties of solid xenon are investigated by low-energy-electron diffraction. Using no adjustable parameters, calculated layer-dependent mean-square vibration amplitudes and scattering factors of solid xenon are used to determine the surface Debye temperature of the xenon (111) face. The magnitude of inelastic electron damping as a function of incident electron energy in solid xenon is also determined. Results of the calculation are compared with experimental measurements for a range of energies from 0 to 400 eV.

I. INTRODUCTION

The study of vibrational modes at surfaces of solids is one of considerable current interest both experimentally and theoretically. Such studies are related to the understanding of the local configuration and interaction potential of ion cores at surfaces. At surfaces of solids, both the microscopic